ACS APPLIED NANO MATERIALS



www.acsanm.org

Article

# Biopolymer-Templated Titania Film Formation for Nanostructured Coatings Revealed by Machine Learning-Supported Time-Resolved Analysis

Julian Eliah Heger, Yufeng Zhai, Shachar Dan, Matthias Schwartzkopf, Ilie Cernev, Calvin J. Gavillet, Nian Li, Tanny Chavez, Alexander Hexemer, Stephan V. Roth, and Peter Müller-Buschbaum*

Cite This: ACS Appl. Nano Mater. 2026, 9, 12970−12979

Read Online

ACCESS | Metrics & More | Article Recommendations | Supporting Information

**ABSTRACT:** This study presents a machine learning approach to derive the film formation of biopolymer-templated titania nanostructures during spray deposition, in combination with in situ grazing-incidence small-angle X-ray scattering (GISAXS). A neural network trained on synthetic GISAXS data directly predicts domain-size distributions from experimental two-dimensional scattering patterns, capturing the full kinetics of nanostructure evolution with high temporal resolution. The predictions reveal hierarchical size distributions and periodic growth features, consistent with layer-by-layer spray deposition and validated by complementary scanning electron microscopy (SEM) imaging. Quantitative comparison with conventional parametric GISAXS fits shows good qualitative agreement, with systematic differences explained by domain-shape assumptions and resolved by applying a geometric scaling factor. Simulated SEM-like surfaces derived from neural network outputs reproduce the porous, foam-like nanoscale morphology observed experimentally, reinforcing the method's credibility. This integrated approach enables real-time, nondestructive, statistically averaged monitoring of bulk nanostructure development in functional coatings, offering a scalable methodology to accelerate the characterization and process control of sustainably manufactured nanostructured titania films for energy-related applications such as photocatalysis and photovoltaics.

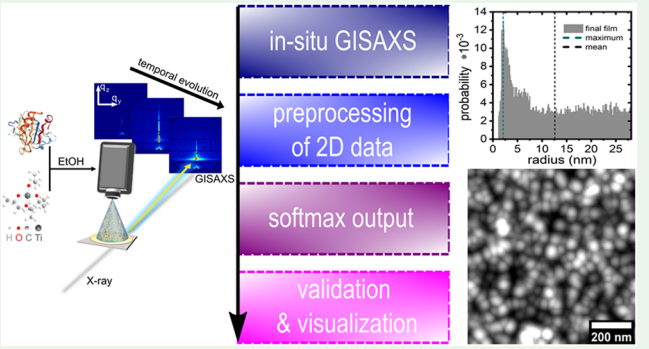


**KEYWORDS:** *nanostructure analysis, machine learning, biopolymer-templated titania, film formation kinetics, neural network analysis*

## INTRODUCTION

Functional nanostructured coatings based on titania find various applications in modern energy materials, such as photocatalytic generation of hydrogen[1−3] and photovoltaics.[4,5] Wet-chemistry synthesis of titania coatings enables scalable fabrication via solution-processing techniques such as spray deposition or printing, aligning with economic interests.[6−8] The performance of the titania coatings crucially depends on their nanostructure and crystallinity.[9,10] Compared to a compact titania coating, porous titania with a tailored nanostructure offers a higher surface-to-volume ratio, thereby increasing the photocatalytic area.[9,11] Among various routes to achieving a nanostructured titania with the desired morphology, block copolymer directed sol−gel synthesis is a particularly successful approach as it meets the conditions for solution processing.[10,11] The use of biopolymers as sustainable templates offers a viable alternative to synthetic polymers. These biomaterials typically facilitate aqueous processing and provide diverse morphologies, e.g., fibrillar or nanoparticles, and functional groups that enable the tailoring of nanostructures and crystallinity in titania films at low temperatures.[6,7,12]

To apply and control the performance of such functional titania coatings, a detailed understanding of the nanostructure and its formation during processing is indispensable. Scanning electron microscopy (SEM) yields an understanding of the porosity, shape, and structure of the surface morphology at the nanoscale. Furthermore, by applying contrast-based algorithms, a size histogram can be easily extracted, counting the number of particles with a given equivalent radius. Such histograms encode information about the nanostructure at a detailed, hierarchical level, making them extremely useful for studying the hierarchical structure of nanostructured titania.[13]

Received: April 13, 2026
Revised: June 9, 2026
Accepted: June 19, 2026
Published: June 26, 2026

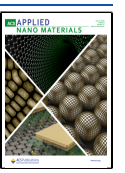

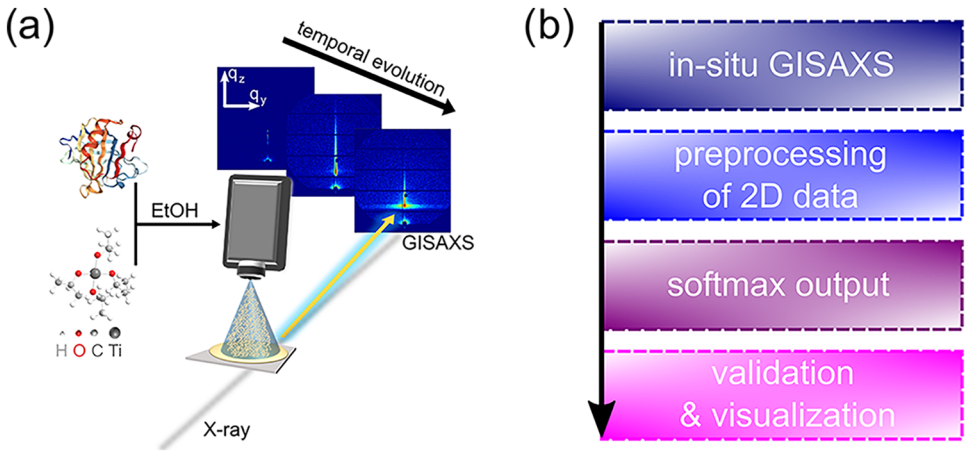


**Figure 1.** (a) Schematic of the in situ GISAXS experimental setup during spray deposition. (b) Experimental workflow including preprocessing and neural network inference.

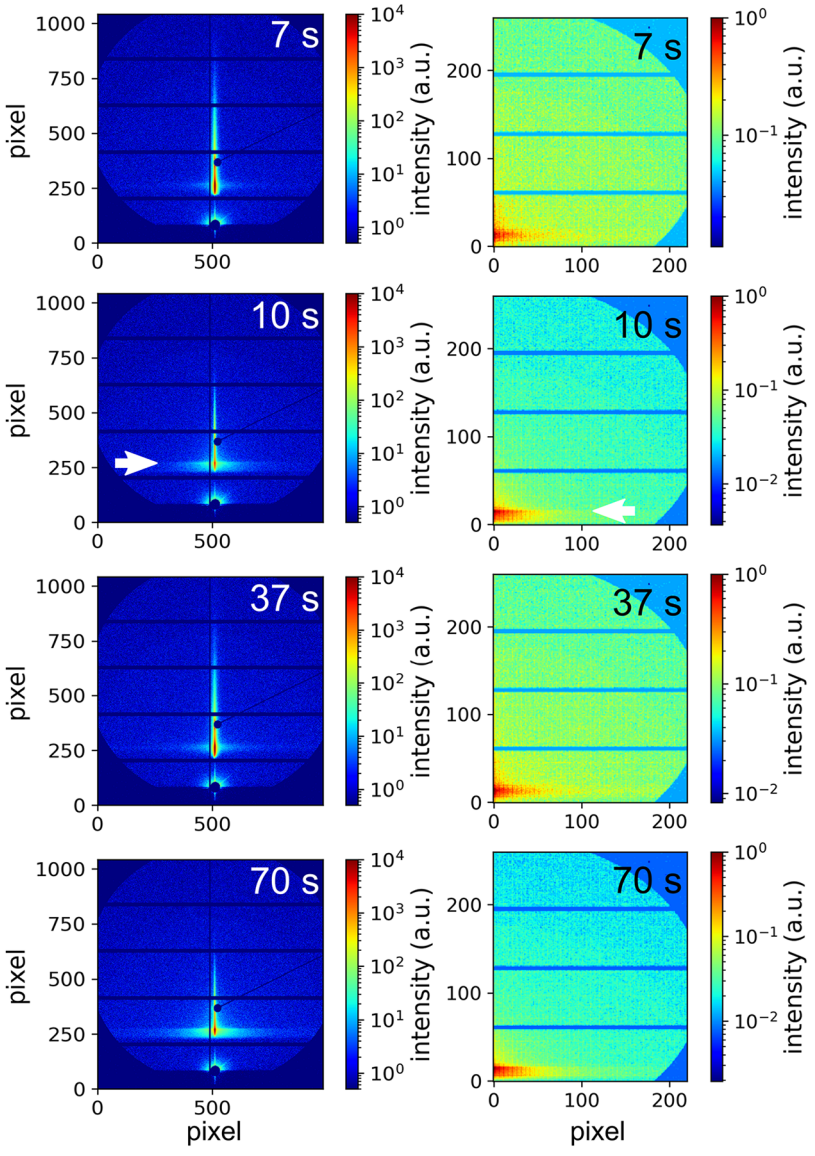


**Figure 2.** Representative 2D GISAXS data before (left column) and after preprocessing (cropping, binning, normalization; right column). The differences in intensity patterns as a function of time stem from the spray pulses (e.g., 7 and 37 s) and drying intervals (e.g., 10 and 70 s), reflecting the complex morphological evolution driven by pulsed spray deposition. To ease preprocessing, the detector images are kept in pixel coordinates. The white arrow marks the Yoneda region with strong diffuse lateral intensity.





https://doi.org/10.1021/acsanm.6c01622
ACS Appl. Nano Mater. 2026, 9, 12970−12979

To obtain real-time information on structure formation and complement SEM imaging, grazing-incidence small-angle X-ray scattering (GISAXS) is an established and powerful tool.[14,15] GISAXS enables following of the fast kinetics during film formation in situ and extends information from surface structures to the bulk, accessing characteristic nanostructures in a statistically significant way.[12,16,17] The nanostructure information is encoded in reciprocal space by two-dimensional (2D) patterns of the scattered intensity. Due to the nature of the ill-posed inverse problem of X-ray scattering, a direct transformation to real space, for instance, with Fourier transformations, is not possible.[18,19] Thus, in order to analyze GISAXS data, parametric models based on analytically solvable form and structure factors are applied to simulate the reciprocal space GISAXS data and compare them with the experimental GISAXS pattern.[20−23] From the applied model parameters, real-space values of size distributions are obtained. While this is a successful strategy, the analysis routine is inherently nontrivial and time-consuming, as reflection and refraction effects arising from the scattering geometry must be accounted for within the distorted-wave Born approximation (DWBA).[24] Furthermore, Monte Carlo regression allows the direct extraction of size histograms from 2D GISAXS patterns needed for further validation with SEM image data and to complement such data.[23,25] Beyond the analysis of a single experiment, a fast, automated route to quantitative nanostructure information is a prerequisite for real-time process monitoring and quality control in the scalable fabrication of nanostructured functional coatings, which will be used for energy-related applications such as photocatalysis and photovoltaics.

To overcome this bottleneck in 2D GISAXS data analysis, we apply a neural network that is trained on synthetic 2D GISAXS data to directly deduce probability densities for nanostructure in terms of sizes, e.g., radii, from experimental 2D GISAXS data.[26−29] The applied network is based on an established and validated geometric model, which successfully describes the growth and film formation of metal clusters on substrates during sputter deposition.[16,17] In the present study, we use this established model directly and apply it in a machine learning network to provide an advanced, quantitative analysis of time-resolved 2D GISAXS data obtained from in situ measurements during the spray deposition of biohybrid titania composite films.[6,12]

During the spray deposition experiment, short spray pulses followed by drying steps ensure a controlled layer-by-layer deposition of the biohybrid film. We use ß-lactoglobulin (ß-lg) as a biotemplate, which is known for its foaming properties for titania as a function of pH and its feasibility to tailor the crystallization of titania within its biomatrix.[6,7,12] As an exemplary case study, we choose a biohybrid solution based on ß-lg and the titania precursor titanium(IV) isopropoxide (TTIP) at a low concentration of 0.1 wt % in a mixed aqueous solution with ethanol (EtOH) as cosolvent. EtOH is applied to control the drying kinetics on the substrate during spray deposition, to stabilize titania precursor TTIP against uncontrolled hydrolysis, and to introduce spherical supramolecular structures by denaturation of ß-lg acting as a template.[30−34] We present an analysis workflow based on the in situ GISAXS experiment, followed by preprocessing of the raw data and input into a neural network predicting probability densities via softmax.[35,36] The predicted results will then be validated against expectations from the literature, an established parametric model, and real-space SEM imaging.[23,37] Finally, the biohybrid film formation is discussed based on the quantitative results. Schematics of the in situ GISAXS experiment and of the analysis workflow are given in Figure 1a,1b, respectively. Experimental details for the in situ GISAXS experiment, the neural network training and application, and the validation and visualization of the predicted results are provided in the Method section.

## RESULTS AND DISCUSSION

### Evaluation of Time-Resolved 2D GISAXS Data Based on a Neural Network

The in situ GISAXS experiments during spray deposition yield real-time information on the nanostructural build-up. The 2D GISAXS data sequence is sorted in a video (see Video 1 in the Supporting Information (SI)). From this sequence, selected 2D GISAXS data are shown in Figure 2. A first qualitative analysis shows the formation of diffuse scattering during deposition, which is evident as strong horizontal intensity lines in the Yoneda region. Further, a periodic oscillation associated with the pulsed spray deposition is revealed, which indicates repeating drying kinetics between surface modifications after a spray pulse every 6 s, see Video 1 (SI).[12,38] This oscillation of the 2D GISAXS data stems from the layer-by-layer deposition with iterative spray cycles (see below Methods section for details) during and directly after spray pulses (e.g., at 7 and 37 s) and the dried state in between spray pulses (e.g., at 10 and 70 s). In total, 850 2D GISAXS data frames are then preprocessed to match the required dimensions of the neural network.[35,36] The preprocessing consists of four steps: (1) cropping of the raw data to a defined region-of-interest (ROI), (2) binning of the detector pixels, (3) normalization of the binned intensities, and (4) an optional clipping step for threshold and background adjustments of the binned intensities. Selected preprocessed 2D GISAXS data are shown in Figure 2. The effect of cropping to a desired ROI is 2-fold. First, it reduces the size of the intensity array by omitting detector areas that contain no relevant scattering information, artifacts, or shadowing elements. Second, it allows for neglecting diffuse scattering in the low $q_y$-regions close to the specular peak and the Yoneda band, see Figure S1, SI. This reduces the complexity of the data analysis for the neural network by avoiding strong intensity variations and the dynamic scattering regime at the cost of a reduced size resolution, limited to the larger $q_y$-region. This approach is a fair compromise, as film formation and early nucleation and growth of building units of hierarchical titania nanostructures typically take place at the larger $q_y$-regions where the neural network is trained on.[12,16,17]

After preprocessing, the 2D GISAXS data is fed into the neural network. The architecture of the neural network is schematically illustrated in Figure S2. A softmax layer outputs the probability density of radii from 1.2 to 28.1 nm, in 0.1 nm steps. An exemplary probability density for the final GISAXS pattern after film formation is shown in Figure S3a. The probability profile shows a rather broad distribution, with a maximum likelihood at a radius of about 2.1 nm and a mean value of about 12.5 nm. We claim that, in good approximation, the softmax probability density can be interpreted as a histogram of the size distributions.[19,25] We validate this interpretation, as the probability density heuristically resembles the expected broad hierarchical distribution of foam-like titania




https://doi.org/10.1021/acsanm.6c01622
ACS Appl. Nano Mater. 2026, 9, 12970−12979

films, which typically exhibit smaller particles of a few nanometers and larger clusters in the tens- to hundreds-of-nanometer range.[6,39−41] Here, the ROI accessible to the neural network cuts of larger sizes than 28.1 nm, else resembling the characteristic size distribution of hierarchical titania. Hence, following our previous work,[6,12,41] we analyze the predicted pseudohistogram with Gaussian functions for each time step to extract the temporal evolution of characteristic radii within a trimodal size distribution. Selected pseudohistograms with indicated maximum and mean values are shown in Figure 3a

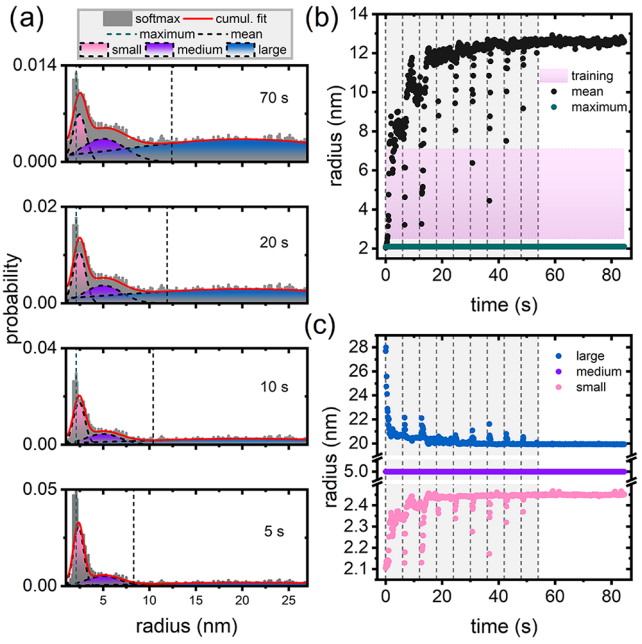


**Figure 3.** Neural network-derived radius predictions. (a) Softmax probability densities at selected times (indicated) and corresponding fits using a trimodal Gaussian distribution. (b) Temporal evolution of neural network-predicted mean and maximum radii. Vertical dashed lines indicate spray pulses that lead to surface modification and structural changes. (c) Temporal evolution of three radius classes, small, medium, and large, extracted via fits of the trimodal Gaussian distribution to the neural network softmax output. Vertical dashed lines indicate spray pulses that lead to surface modification and structural changes.

together with the Gaussian fits. Apparently, the maximum probability remains around 2.1 nm, while the mean value shifts toward higher values with ongoing spray deposition. This behavior indicates that the main structural components of the biohybrid film are small subunit building blocks that hierarchically condense into larger structures upon drying.[6,12,41] A detailed evolution of the maximum and mean values is shown in Figure 3b, where the training region of the neural network is also indicated. We observe that the neural network is able to predict values well beyond the training scope and, at the same time, identifies a sigmoidal growth of the radius associated with the mean probability. Furthermore, a periodic change in this radius occurs at the given time of an individual spray pulse, reflecting the layer-by-layer deposition, revealing characteristic deposition features, which the neural network supports, validating their validity[42] and furthermore corroborates the advantage of using neural networks for analyzing drying kinetics.[43] Figure 3c shows the temporal evolution of the predicted results as extracted from the Gaussian fits. We observe a slight sigmoidal growth of the small structure from about 2.06 nm to about 2.45 nm within the first 18 s of deposition. The medium structure remains constant and unaffected by deposition, and remains approximately constant at about 5 nm. The large structure shows an exponential shrinking from about 28 nm to about 20 nm within the 24 s of deposition. We note that the neural network correctly identifies the periodic nature of size evolution during the repeating spray pulses. Further spray pulses add relatively less and less material to the already established structure, as both the bulk and the surface are probed by GISAXS, and all three characteristic structures eventually reach a quasi-steady state. The overall evolution of the predicted domain sizes, that is, growth of smaller and shrinking of larger domains, qualitatively reflects what is expected from previous studies on spray-deposited titania nanostructures and suggests crystal growth within an amorphous matrix upon condensation and hierarchical assembly of larger aggregates.[6,7,12]

## Validation and Visualization of the Predicted Results

While the predicted results qualitatively match the expected film formation and consistently reveal characteristic deposition features, a more quantitative validation using established GISAXS analysis routines is of crucial importance for verifying the neural network analysis. For this, we apply a parametric model based on spherical form factors to describe the one-dimensional (1D) horizontal linecuts taken at the Yoneda band in the 2D GISAXS data. This model-fit approach is state-of-the-art in GISAXS analysis for extracting lateral domain sizes and serves as a ground-truth comparison.[23] Figure 4a shows selected linecuts together with the model fits stacked along the vertical axis for clarity. The linecuts contain all information in the full $q_y$-region as obtained from the in situ GISAXS experiment. In addition, the reduced resolution of the

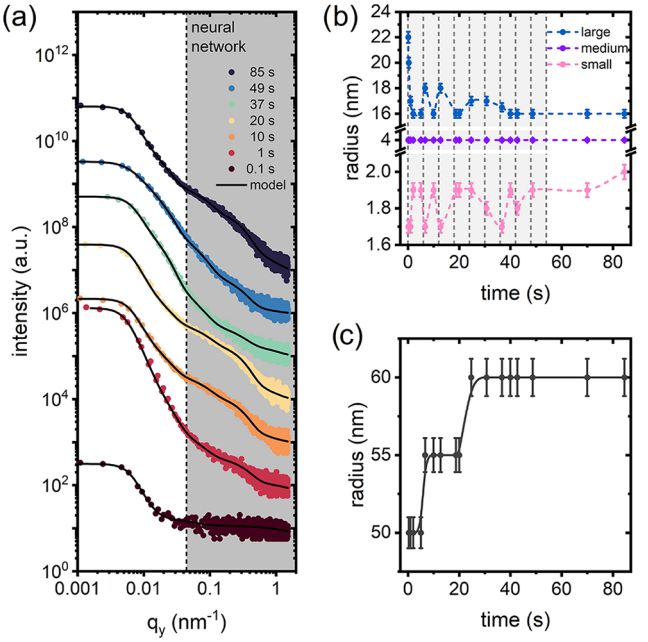


**Figure 4.** Parametric validation using spherical form factors. (a) Horizontal line cuts with model fits at selected times. (b) Temporal evolution of effective radii extracted from the parametric model. (c) Additional large-scale structure not resolved by the neural network due to ROI-limited reciprocal-space coverage after preprocessing.





https://doi.org/10.1021/acsanm.6c01622
ACS Appl. Nano Mater. 2026, 9, 12970−12979

neural network due to ROI-cropping is indicated by dashed lines. The gray area shows the valid ROI for the neural network training and analysis. The parametric model fits reveal a hierarchical size distribution consisting of four characteristic structures: three characteristic structures within the neural network resolution (Figure 4b) and a fourth (Figure 4c), largest structure, which is not accessible to the neural network due to ROI cropping to reduce complexity. Figure 4b shows the growth of the small structure from about (1.70 ± 0.03) nm to about (2.00 ± 0.04) nm for selected deposition times. A periodic variation in the small radius is observed, as expected from pulsed deposition, since each pulse induces surface modifications and structural changes comparable to those observed in earlier stages of film formation. This effect diminishes as the bulk contribution to the scattering pattern dominates over the surface contribution. The medium structure remains constant at about (4.00 ± 0.08) nm. The large structure shrinks from about (22.00 ± 0.44) nm to about (16.00 ± 0.32) nm, also showing a periodic feature referred to as the pulsed deposition. The evolution of the largest structure (Figure 4c) reflects a pseudosigmoidal growth from about (50.0 ± 1.0) nm to about (60.0 ± 1.2) nm. Overall, the size distribution obtained from the parametric model captures the general trend of the histogram obtained from SEM imaging (Figure S3b,c, Supporting Information, respectively). The in situ GISAXS time series captures the structural evolution during increasing film thickness. Each measurement after a spray pulse corresponds to an increased amount of deposited material, providing thickness-dependent structural information from within a single, continuous deposition process. The vertical film profile obtained from the intensity line cut along $q_z$ of the final, equilibrated film shows no indication of enrichment layers forming during deposition, consistent with a film that grows homogeneously along the surface normal under the layer-by-layer protocol used in this work (Figure S4). The density of data points from the parametric model is lower than the predicted values, as only a selected subset of the 2D GISAXS data has been used, restricted to representative time steps, similar to our previous work.[43] Besides the largest structure, which is not accessible to the neural network, a qualitative comparison of the temporal evolution of the results from the parametric model and the predicted results from the neural network shows a good agreement. Quantitatively, however, the parametric model yields overall smaller sizes as predicted by the neural network.

To further illuminate this quantitative discrepancy, we analyze the ratio of the radii from the parametric results and the neural-network predicted results (Figure 5a). The obtained radius ratios for all three characteristic structures scatter closely around a constant value of 0.8. We know from previous studies that a constant ratio strongly indicates a geometric correlation between domains.[12] In this particular case, the obvious difference between predicted values and model-fitted values is the applied form factor: while the neural network was generically trained on well-established hemispherical domain shapes (see Methods section), the model-fit applies spherical shapes.[16,17] Given the fact that the raw 2D GISAXS data encodes the same material density independent of the analysis routine, we suggest that the constant ratio reflects a volumetric transformation from hemispheres with radius $r_{hemi}$ to full spheres with radius $r_{sph}$[17]

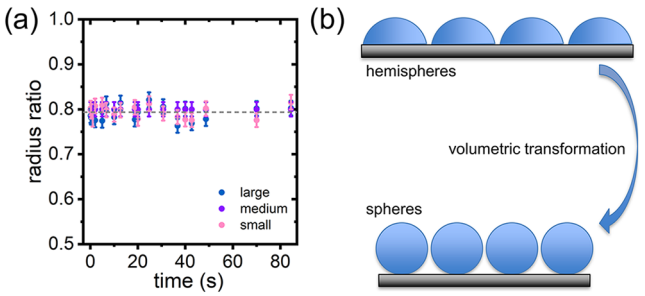


**Figure 5.** Geometry-based scaling between predicted and parametric radii. (a) Ratio of neural network-predicted radii to parametric-model radii around 0.8, consistent with geometry mismatch. (b) Schematic illustration of volumetric transformation between hemispherical (training) and spherical (validation) form factors.

$$\frac{2}{3}\pi r_{hemi}^3 = \frac{4}{3}\pi r_{sph}^3 \Rightarrow \frac{r_{sph}}{r_{hemi}} = 2^{-1/3} \approx 0.794 \quad (1)$$

perfectly matching the observed radius ratio as indicated by the dashed line in Figure 5a. This finding provides a physically grounded calibration rule: Once the form factor is established in independent experiments (e.g., approximately spherical domains supported by SEM), the neural network-predicted hemispherical radii can be mapped to spherical radii while preserving the high-temporal-resolution pulse signatures of the in situ GISAXS experiments (Figure 5b). Furthermore, this finding highlights the robustness of the neural network trained on hemispheres. Importantly, such an approach may significantly reduce the number of specially trained models required to analyze similar in situ GISAXS experiments.

Based on neural network predictions and interpreting the softmax output as a pseudohistogram, it is now possible to simulate SEM-like surfaces and compare these real-space structures to experimental SEM data. Figure 6a shows the simulated topography of the biohybrid titania nanostructures after spray deposition. The visualization shows a porous

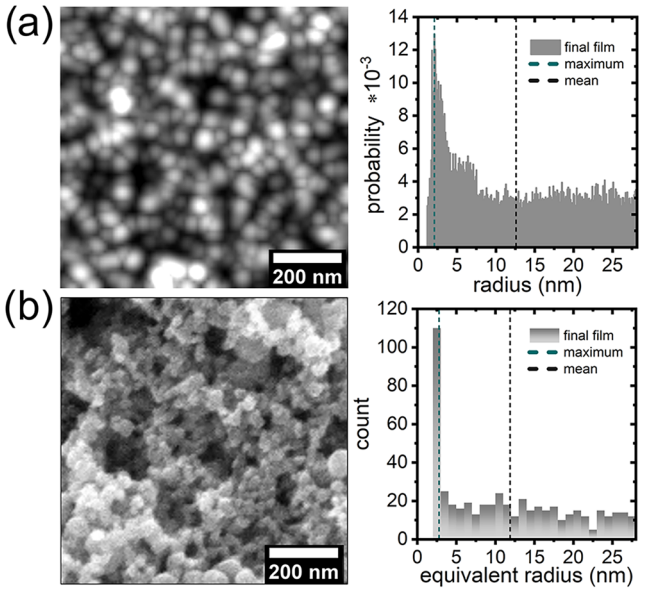


**Figure 6.** SEM consistency check. (a) Simulated SEM image based on neural network predictions. (b) Experimental SEM data and corresponding histogram, showing qualitative and quantitative agreement with neural network-derived size statistics.





https://doi.org/10.1021/acsanm.6c01622
ACS Appl. Nano Mater. 2026, 9, 12970−12979

nanostructure with hierarchically assembled spherical domains. The irregular and loose, porous network matches expectations for a typical foam-like titania film.[6,9,12] Comparing the simulation with experimental SEM data (Figure 6b) in the same size range, the qualitative agreement between the predicted simulation and real-space structure becomes apparent. For a quantitative comparison, a size histogram of equivalent radii is obtained from the experimental SEM data and compared with the predicted pseudohistogram, which has a maximum value of 2.1 nm and a mean value of 12.6 nm. The experimental histogram agrees with the prediction in terms of the maximum counts at a low radius of about 2.8 nm and a mean radius of about 11.9 nm with a broad, hierarchical size distribution, further validating the neural network results. For comparison of the ROI sizes, the experimental SEM histogram in Figure 6b is limited to structures up to 28.1 nm. While the statistics are inherently different between local probe methods, such as SEM, and statistically averaging methods, such as GISAXS, the individual counts per size may differ. However, we observe consistent values for the maximum and mean.

Together with the SEM-based real-space validation discussed in Figure 6, and the agreement of the neural-network, parametric-model, and SEM-derived size distributions shown in Figure S3, this parameter-free geometric prediction provides a cross-method validation of the calibration factor across reciprocal-space scattering, geometric reasoning, and real-space imaging.

## On the Generality and Limitations of the Neural Network Prediction

While the neural network demonstrates robust performance in the biopolymer-templated titania system studied here, its generality and current limitations should be considered. As the model is trained on synthetic GISAXS data, the approach is transferable to other scattering systems and can, in principle, be retrained for different sample geometries, scattering-vector ranges, and material systems. The main current limitations follow from the training data and the network architecture. First, the structure-factor contribution was neglected during training, which is justified for the foam-like morphology under investigation, where no significant interdomain correlation is observed, but would likely not hold for spatially correlated systems. Second, the synthetic training patterns are generated for isotropic morphologies with hemispherical form factors. In combination with the fully connected, dense architecture applied in this work, strongly anisotropic form factors or morphologies, such as oriented rods or lamellar arrangements, would likely not be adequately represented. Their analysis would require both adapted training data and an architecture that preserves angular information in the 2D GISAXS data. Within these constraints, the multimodal and hierarchical size distributions retrieved here for the biopolymer-templated titania composite demonstrate that the approach is not limited to the unimodal Gaussian shape used in the training labels as the network learns to combine the basis distributions into the observed multimodal pseudohistograms. Finally, while the predictions are validated here for the titania:ß-lg composite, their application to chemically distinct material systems should be independently validated.

## Biohybrid Film Formation During Spray Deposition

Biohybrid film formation during the spray deposition of ß-lg and TTIP in aqueous ethanol involves a complex interplay of chemical and physical processes governed by sol−gel chemistry and biopolymer templating.[44] Ethanol serves as a critical cosolvent that modulates the hydrolysis rate of TTIP, effectively slowing down its rapid hydrolysis and precipitation, observed in purely aqueous systems.[30] This controlled hydrolysis facilitates the nucleation and growth of stable anatase-$TiO_2$ nanoparticles with an approximate radius of 2 nm, preventing uncontrolled aggregation and ensuring uniform particle size distribution.[9,30,45] The presence of ß-lg, a biopolymer with inherent foaming and templating properties, provides a supramolecular scaffold that directs the spatial organization of these primary titania nanoparticles into a hierarchical, foam-like porous network.[6,7,12] This network is characterized by a multimodal pore-size distribution, in which smaller nanoparticles aggregate into medium-sized domains (∼5 nm) and further condense into larger porous structures that initially measure around 28 nm but shrink to approximately 20 nm due to densification during drying.

The spray deposition process itself is pulsed, inducing cyclical wetting and drying phases that are reflected in oscillations in domain sizes, as detected by machine learning-supported GISAXS analysis. These cycles promote a layer-by-layer growth mechanism whereby newly formed nanoparticles and aggregates deposit onto previously formed layers, followed by drying-induced densification and reorganization.[12,38] This kinetic process leads to the gradual evolution of the film's nanostructure, with smaller subunits growing and larger domains shrinking in size, consistent with sol−gel condensation kinetics and templated assembly. This characteristic evolution is associated with crystal growth during drying within an amorphous, condensing network.[12] The aqueous ethanol solvent system not only moderates TTIP hydrolysis but also accelerates evaporation rates compared to pure water, providing a controlled drying environment that supports the hierarchical assembly and stabilization of the porous architecture.[30,32,33]

The resulting biohybrid film exhibits anatase-$TiO_2$ crystallinity, a desirable phase for photocatalytic and functional applications, as confirmed by complementary ex-situ grazing-incidence wide-angle X-ray scattering (GIWAXS, Figure S5).[9,45] GIWAXS reveals the (101) anatase reflex,[46] from which a lower limit for the crystal coherence length $L_{101} \approx 3.1$ nm is estimated by Scherrer analysis,[47] agreeing with the small structure from GISAXS.[9,12,45] The hierarchical porous morphology, driven by ß-lg templating and solvent effects, significantly enhances the surface area and accessibility of the titania network, which is critical for optimizing the material's photocatalytic efficiency and other surface-dependent functionalities.[6,41,48] This film formation mechanism aligns well with established principles from the literature on titania sol−gel synthesis and biopolymer templating, where controlled hydrolysis, biopolymer-induced conformational templating, and solvent-mediated drying kinetics collectively govern the formation of nanostructured, porous films.[6,7,12] Controlled hydrolysis regulates the precursor reactions essential for film development, while biopolymer-induced conformational templating directs the nanoscale architecture through molecular guidance.[30,32] Additionally, solvent-mediated drying kinetics influence the pore structure and overall morphology during film solidification.[34,41] Overall, the integration of ß-lg biotemplating with controlled sol−gel chemistry in an aqueous ethanol medium during pulsed spray deposition enables the fabrication of biohybrid films with finely tuned hierarchical





https://doi.org/10.1021/acsanm.6c01622
ACS Appl. Nano Mater. 2026, 9, 12970−12979

porosity and crystalline phases, suggesting controlled functional properties.

## CONCLUSIONS

This study presents an integration of machine learning with time-resolved 2D GISAXS measurements to analyze the nanostructure formation of biopolymer-templated titania coatings during spray deposition. By using a neural network trained on synthetic GISAXS data, the approach enables direct prediction of domain-size distributions as a function of time from experimental 2D GISAXS data, capturing the details of the kinetics of nanostructure evolution with high temporal resolution. The neural network predictions reveal characteristic hierarchical size distributions and periodic growth features corresponding to the pulsed deposition process, which are consistent with expectations from previous studies and supported by complementary SEM imaging.

Quantitative validation against conventional parametric GISAXS fits demonstrates a good qualitative agreement, with systematic differences attributable to the distinct domain shape assumptions used in training and modeling. A physically grounded geometric scaling factor reconciles these differences, highlighting the robustness and transferability of the neural network approach. Furthermore, simulation of SEM-like surfaces from neural network outputs reproduces the porous, foam-like morphology observed experimentally, reinforcing the validity and stability of the machine learning-supported analysis.

Overall, this integrated approach, combining machine learning with in situ scattering techniques, offers a comprehensive method for analyzing nanostructure evolution in biopolymer-templated titanium films, overcoming time limitations of traditional microscopy and parametric modeling by enabling real-time, nondestructive, and statistically averaged monitoring of bulk nanostructure development in functional coatings. The successful application of machine learning-supported GISAXS analysis provides a scalable, sustainable methodology to accelerate the characterization and optimization of energy-relevant nanomaterials, advancing the understanding and design of biopolymer-templated titania films. The presented approach is particularly suited for real-time process monitoring and quality control in the sustainable, water-based fabrication of nanostructured functional coatings for energy-related applications.

## METHODS

### Preparation of Biohybrid Solutions

Aqueous solutions of 0.1 wt % ß-lg were adjusted to pH 2 by the addition of 1 M HCl. The resulting two protein solutions were sealed in glass vials and heat denatured by thermal treatment at 90 °C for 24 h while continuously stirring.[31,34,49] After that, the titania precursor TTIP (diluted to 0.1 wt % in EtOH) was added dropwise to the final heat-denatured protein solutions under continuous stirring.

### In Situ GISAXS Measurement During Spray Deposition of Biohybrid Titania

To reveal the structure formation of the biohybrid films, in situ GISAXS was performed during pulsed spray deposition. The GISAXS intensity depends both on the size of the scattering domains, via the form factor, and on the film density, via the interfacial scattering contrast $\Delta\rho$ and the position of the Yoneda peak (eq S1 and Figure S1). An air-atomizing spray nozzle (JAUCO D555000, Spraying System Co, Hamburg, Germany) was installed in a custom-built spray chamber with a nozzle-to-substrate distance of 23 cm. A 2 × 2 $cm^2$ silicon wafer (Si-Mat, Germany) was used as a substrate and heated to 80 °C. Nitrogen at 1 bar pressure was used as a carrier gas for the biohybrid solution. Each of the applied 10 spray pulses lasted 0.1 s and was followed by 5.9 s of drying. After that, the 10 spray pulses, the sample rested for 25 s to complete drying, so that the in situ GISAXS experiment lasted a total of 85 s. The in situ GISAXS measurements were performed at the beamline P03 MiNaXS of the storage ring PETRA III (DESY, Hamburg, Germany).[50] The layer-by-layer formation was recorded with a Pilatus 1 M detector (pixel size 0.172 × 0.172 $mm^2$) at a distance of 3410 mm from the sample. The incident angle was set to 0.4° with respect to the incoming X-ray beam with an energy of 11.7 keV.[50,51] The frame rate of the PILATUS 1 M detector was set to 10 Hz, yielding a total of 850 images per sample during deposition.

### Preprocessing of 2D GISAXS Data

Before the raw 2D GISAXS data was provided to the neural network to predict film formation during spray deposition, preprocessing steps were applied. These steps began with cropping the full image to a certain region of interest and binning of the detector pixels. Subsequently, the pixel intensities were normalized according to

$$I_{\text{norm}} = \frac{I - I_{\text{min}}}{I_{\text{max}} - I_{\text{min}}} \tag{2}$$

where $I_{\text{norm}}$ is the normalized intensity, $I$ is the raw intensity of each pixel in the 2D GISAXS data, and $I_{\text{min}}$ and $I_{\text{max}}$ are the minimum and maximum values of the raw intensity, respectively. A workflow of data preprocessing is shown in Figure S6, SI, including more detailed information.

### Model Training and Architecture of Neural Network

Data labeling and training involved generating precise annotations for data sets to facilitate the effective development of machine learning models.[27,52] Following the workflow in Figure S6, labels were created by generating one-hot encoded vectors corresponding to features such as radius and its standard deviation $\sigma_R$, with dimensions tailored to the simulation data. This labeling process differentiated between experimental and simulation data, with additional labels for $\sigma_R$ generated exclusively for simulations. The labeled data set, comprising simulated 2D GISAXS patterns along with their respective one-hot labels, formed the foundation for model training. Accurate labeling was crucial for enabling models to learn appropriate feature distinctions, thereby enhancing their accuracy and robustness throughout the training process. The neural network was trained on simulation data to compensate for the scarcity of experimental training examples, focusing on predicting the average structure radius. The analysis focused solely on radii, as we did not observe a characteristic structural correlation between the foam-like domains, as we did in earlier work.[6] Thus, the structure factor contribution was neglected. A multilayer dense network with two hidden layers was trained on 17229 labeled examples derived from simulated GISAXS data. The training data was generated using the IsGISAXS software,[20] using hemispherical form factors with a Gaussian size distribution for supported gold nanoparticles with strong scattering contrast with respect to the Si substrate, which offers a generic model to analyze nanostructures.[16,20] The training was limited to simulations with a fixed relative spread of radius $R$ ($\sigma_R/R$ = 30%). The preprocessed intensity arrays were transferred as a vector of length 57200 to the first hidden layer, a leaky ReLU with 1024 nodes and an activation of $x$ = 0.03. The data then proceeded to the second hidden layer, a ReLU with 504 nodes. Eventually, predictions were provided through the softmax output as a vector of length 270, containing the probability distributions of the predicted radii for each 2D GISAXS data, enabling weighted averages for parameter estimation. We note that the training model was initially developed for hemispherical gold nanoparticles on a Si substrate[16] and used without further modification or adaptation to reduce complexity. The good agreement between neural network predictions and complementary experimental results demonstrates the general validity of the model, justifying its direct use.





https://doi.org/10.1021/acsanm.6c01622
ACS Appl. Nano Mater. 2026, 9, 12970−12979

The cropped and binned 2D GISAXS pattern is provided to the network as a flattened one-dimensional intensity vector of length 57,200. We note that the 2D GISAXS pattern is not radially symmetric, even for an isotropic real-space morphology, owing to the distinct roles of the horizontal ($q_y$) and vertical (qz) directions in the grazing-incidence geometry. Flattening into a one-dimensional input is nevertheless justified here because the spatial position of each detector bin in the ($q_y$, $q_z$) raster is fixed and identically mapped for every training and inference example. The fully connected architecture learns a separate weight for each bin and therefore retains the relevant information from the 2D pattern. What the architecture does not exploit is translational weight-sharing, an inductive bias well suited to translation-invariant local motifs in natural images but not required for the ($q_y$, $q_z$)-structured GISAXS intensity. This justification holds for the isotropic real-space morphology of the biopolymer-templated titania, foam-like composite considered here. Physically anisotropic systems with azimuthal intensity variations stemming from a preferred orientation in the sample would likely require an architecture that preserves angular information together with adapted training data.

### Simulation of SEM-like Surface from Softmax Prediction

A physics-based simulation was developed to generate synthetic SEM images from neural network–predicted particle size distributions, linking GISAXS reciprocal-space data to real-space SEM observations. Particles were randomly placed in a $(1000\ nm)^3$ cubic volume with radii sampled from predictions. Each particle's contribution to a 3D voxel grid was modeled using a Gaussian density weighted by particle volume to reflect secondary electron yield. Gaussian parameters were chosen to mimic realistic SEM imaging characteristics, including gradual intensity transitions and typical interaction volumes. A 3D Gaussian smoothing simulated detector blurring, and the final 2D SEM-like image was produced by maximum intensity projection along the beam axis. This approach effectively captures overlapping particles and sample depth effects. More details are provided in the SI.

### Experimental SEM Validation

For morphological validation of the neural-network predictions, SEM is used as a real-space probe complementary to reciprocal GISAXS. SEM resolves the foam-like domain network at the relevant length scale and is well suited to spray-deposited biohybrid films, which combine pronounced macroscopic roughness from the pulsed deposition with a soft, hierarchical biopolymer-templated nanostructure. The SEM measurements were performed at a working distance of 3.5 mm and an accelerating voltage of 5 kV (Zeiss NVision 40).

## ■ ASSOCIATED CONTENT

### Data Availability Statement

All relevant data are included in the paper and its Supporting Information. The data can also be found at the following public repository: 10.14459/2026mp1855186

### Supporting Information

The Supporting Information is available free of charge at https://pubs.acs.org/doi/10.1021/acsanm.6c01622.

Model architecture; additional size histograms; 2D GIWAXS data; and workflow of data labeling and preprocessing (PDF)

GISAXS analysis; simulation of SEM-like surface; and in situ 2D GISAXS data (MP4)

## ■ AUTHOR INFORMATION


### Corresponding Author

**Peter Müller-Buschbaum** − *Technical University of Munich, TUM School of Natural Sciences, Department of Physics, Chair for Functional Materials, 85748 Garching, Germany;* orcid.org/0000-0002-9566-6088; Email: muellerb@ph.tum.de

### Authors

**Julian Eliah Heger** − *Technical University of Munich, TUM School of Natural Sciences, Department of Physics, Chair for Functional Materials, 85748 Garching, Germany;* orcid.org/0000-0001-7719-0111

**Yufeng Zhai** − *Deutsches Elektronen-Synchrotron DESY, 22607 Hamburg, Germany;* orcid.org/0009-0005-3187-1815

**Shachar Dan** − *Deutsches Elektronen-Synchrotron DESY, 22607 Hamburg, Germany*

**Matthias Schwartzkopf** − *Deutsches Elektronen-Synchrotron DESY, 22607 Hamburg, Germany;* orcid.org/0000-0002-2115-9286

**Ilie Cernev** − *Technical University of Munich, TUM School of Natural Sciences, Department of Physics, Chair for Functional Materials, 85748 Garching, Germany*

**Calvin J. Gavillet** − *Deutsches Elektronen-Synchrotron DESY, 22607 Hamburg, Germany; Department of Fibre and Polymer Technology, KTH Royal Institute of Technology, 114 28 Stockholm, Sweden*

**Nian Li** − *Technical University of Munich, TUM School of Natural Sciences, Department of Physics, Chair for Functional Materials, 85748 Garching, Germany; School of Physics, University of Electronic Science and Technology of China, Chengdu 610106, China;* orcid.org/0000-0003-4051-5976

**Tanny Chavez** − *Advanced Light Source,, Lawrence Berkeley National Laboratory, Berkeley, California 94720, United States*

**Alexander Hexemer** − *Advanced Light Source,, Lawrence Berkeley National Laboratory, Berkeley, California 94720, United States*

**Stephan V. Roth** − *Deutsches Elektronen-Synchrotron DESY, 22607 Hamburg, Germany; Department of Fibre and Polymer Technology, KTH Royal Institute of Technology, 114 28 Stockholm, Sweden;* orcid.org/0000-0002-6940-6012

Complete contact information is available at: https://pubs.acs.org/10.1021/acsanm.6c01622


### Author Contributions

The manuscript was written through the contributions of all authors. All authors have given approval to the final version of the manuscript.

### Notes

The authors declare no competing financial interest.

## ■ ACKNOWLEDGMENTS

We acknowledge support by funding from the Bundesministerium für Forschung, Technologie und Raumfahrt (BMFTR) (former: Bundesministerium für Bildung und Forschung) for funding in the framework ErUM Data initiative via grant numbers 05D23WO1 and 13D22CH7 "Versatile Inverse Problem Framework (VIPR) and from the Deutsche Forschungsgemeinschaft (DFG, German Research Foundation) project MU1487/32 and Germany's Excellence Strategy EXC 2089/1−390776260 (e-conversion), from the Bayerisches Staatsministerium für Wissenschaft und Kunst via TUM.solar in the context of the Bavarian Collaborative

Research Project Solar Technologies Go Hybrid (SolTech), as well as from the Center for NanoScience (CeNS). The authors acknowledge DESY (Hamburg, Germany), a member of the Helmholtz Association HGF, for the provision of experimental facilities. Parts of this research were carried out at PETRA III. Data was collected using beamline P03 provided by DESY Photon Science, and we would like to thank P03 staff and Roy Schaffrina for assistance during the experiments. The authors thank Prof. Alexander Holleitner and Claudia Paulus for providing access to the scanning electron microscope. N.L. thanks the funding from the National Natural Science Foundation of China (Grant No. 12504085), Natural Science Foundation of Sichuan Province (Grant No. 2025ZNSFSC0861), and Fundamental Research Funds for the Central Universities (Grant No. ZYGX2024XJ044). Tanny Chavez and Alexander Hexemer were supported by the Advanced Light Source, a U.S. DOE Office of Science User Facility under contract no. DE-AC02-05CH11231.

## REFERENCES

(1) Coward, L. T.; Chu, T. T. M.; Li, X.; Lyu, P.; Love, O. Surface or Bulk? Mechanistic Insights into $Ni^{2+}$-Doped Brookite $TiO_2$ Photocatalysts. *ACS Nanosci. Au* **2025**, *5* (4), 324−336.

(2) Bhom, F.; Isa, Y. M. Photocatalytic Hydrogen Production Using $TiO_2$-based Catalysts: A Review. *Global Challenges* **2024**, *8* (11), No. 2400134.

(3) Rafique, M.; Hajra, S.; Irshad, M.; Usman, M.; Imran, M.; Assiri, M. A.; Ashraf, W. M. Hydrogen Production Using $TiO_2$-Based Photocatalysts: A Comprehensive Review. *ACS Omega* **2023**, *8* (29), 25640−25648.

(4) Ballabio, M.; Cánovas, E. Electron Transfer at Quantum Dot-Metal Oxide Interfaces for Solar Energy Conversion. *ACS Nanosci. Au* **2022**, *2* (5), 367−395.

(5) Jeong, I.; Park, Y. H.; Bae, S.; Park, M.; Jeong, H.; Lee, P.; Ko, M. J. Solution-Processed Ultrathin $TiO_2$ Compact Layer Hybridized with Mesoporous $TiO_2$ for High-Performance Perovskite Solar Cells. *ACS Appl. Mater. Interfaces* **2017**, *9* (42), 36865−36874.

(6) Heger, J. E.; Reitenbach, J.; Kreuzer, L. P.; Pan, G.; Tian, T.; Huber, L. F.; Li, N.; Sochor, B.; Schwartzkopf, M.; Roth, S. V.; Koutsioubas, A.; Müller-Buschbaum, P. Tuning the Morphology of Spray-Coated Biohybrid Beta-lactoglobulin:TiBALDh Films with pH for Water-Based and Nanostructured Titania. *JACS Au* **2025**, *5* (4), 1894−1902.

(7) Huber, L. F.; Sun, K.; Reus, M. A.; Weindl, C. L.; Heger, J. E.; Roth, S. V.; Müller-Buschbaum, P. Beta-Lactoglobulin for Water-Based and Tunable Nanostructure Templating of Printed Titania Thin Films: The Influence of pH Value and Protein Concentration. *Adv. Mater. Interfaces* **2025**, *12* (13), No. 2400929, DOI: 10.1002/admi.202400929.

(8) Maleki, H.; Bertola, V. $TiO_2$ Nanofilms on Polymeric Substrates for the Photocatalytic Degradation of Methylene Blue. *ACS Appl. Nano Mater.* **2019**, *2* (11), 7237−7244.

(9) Bleta, R.; Alphonse, P.; Lorenzato, L. Nanoparticle Route for the Preparation in Aqueous Medium of Mesoporous $TiO_2$ with Controlled Porosity and Crystalline Framework. *J. Phys. Chem. C* **2010**, *114* (5), 2039−2048.

(10) Sarkar, A.; Jeon, N. J.; Noh, J. H.; Seok, S. I. Well-Organized Mesoporous $TiO_2$ Photoelectrodes by Block Copolymer-Induced Sol−Gel Assembly for Inorganic−Organic Hybrid Perovskite Solar Cells. *J. Phys. Chem. C* **2014**, *118* (30), 16688−16693.

(11) Nedelcu, M.; Lee, J.; Crossland, E. J. W.; Warren, S. C.; Orilall, M. C.; Guldin, S.; Hüttner, S.; Ducati, C.; Eder, D.; Wiesner, U.; Steiner, U.; Snaith, H. J. Block Copolymer Directed Synthesis of Mesoporous $TiO_2$ for Dye-Sensitized Solar Cells. *Soft Matter* **2009**, *5* (1), 134−139.

(12) Heger, J. E.; Chen, W.; Yin, S.; Li, N.; Körstgens, V.; Brett, C. J.; Ohm, W.; Roth, S. V.; Müller-Buschbaum, P. Low-Temperature and Water-Based Biotemplating of Nanostructured Foam-Like Titania Films Using ß-Lactoglobulin. *Adv. Funct. Mater.* **2022**, *32* (20), No. 2113080, DOI: 10.1002/adfm.202113080.

(13) Mandlmeier, B.; Szeifert, J. M.; Fattakhova-Rohlfing, D.; Amenitsch, H.; Bein, T. Formation of Interpenetrating Hierarchical Titania Structures by Confined Synthesis in Inverse Opal. *J. Am. Chem. Soc.* **2011**, *133* (43), 17274−17282.

(14) Hexemer, A.; Müller-Buschbaum, P. Advanced Grazing-Incidence Techniques for Modern Soft-Matter Materials Analysis. *IUCrJ* **2015**, *2* (Pt 1), 106−125.

(15) Mahmood, A.; Wang, J.-L. A Review of Grazing Incidence Small- and Wide-Angle X-Ray Scattering Techniques for Exploring the Film Morphology of Organic Solar Cells. *Sol. RRL* **2020**, *4* (10), No. 2000337, DOI: 10.1002/solr.202000337.

(16) Schwartzkopf, M.; Buffet, A.; Körstgens, V.; Metwalli, E.; Schlage, K.; Benecke, G.; Perlich, J.; Rawolle, M.; Rothkirch, A.; Heidmann, B.; Herzog, G.; Müller-Buschbaum, P.; Röhlsberger, R.; Gehrke, R.; Stribeck, N.; Roth, S. V. From Atoms to Layers: In Situ Gold Cluster Growth Kinetics During Sputter Deposition. *Nanoscale* **2013**, *5* (11), 5053−5062.

(17) Schaper, S. J.; Löhrer, F. C.; Xia, S.; Geiger, C.; Schwartzkopf, M.; Pandit, P.; Rubeck, J.; Fricke, B.; Frenzke, S.; Hinz, A. M.; Carstens, N.; Polonskyi, O.; Strunskus, T.; Faupel, F.; Roth, S. V.; Müller-Buschbaum, P. Revealing the Growth of Copper on Polystyrene-Block-Poly(Ethylene Oxide) Diblock Copolymer Thin Films With In Situ GISAXS. *Nanoscale* **2021**, *13* (23), 10555−10565.

(18) Gommes, C. J.; Jaksch, S.; Frielinghaus, H. Small-Angle Scattering for Beginners. *J. Appl. Crystallogr.* **2021**, *54* (Pt 6), 1832−1843.

(19) Leng, K.; King, S.; Snow, T.; Rogers, S.; Markvardsen, A.; Maheswaran, S.; Thiyagalingam, J. Parameter Inversion of a Polydisperse System in Small-Angle Scattering. *J. Appl. Crystallogr.* **2022**, *55* (Pt 4), 966−977.

(20) Lazzari, R. IsGISAXS: A Program for Grazing-Incidence Small Angle X-Ray Scattering Analysis of Supported Islands. *J. Appl. Crystallogr.* **2002**, *35*, 406−421.

(21) Babonneau, D. FitGISAXS: Software Package for Modelling and Analysis of Gisaxs Data Using Igor Pro. *J. Appl. Crystallogr.* **2010**, *43* (4), 929−936.

(22) Pospelov, G.; van Herck, W.; Burle, J.; Carmona Loaiza, J. M.; Durniak, C.; Fisher, J. M.; Ganeva, M.; Yurov, D.; Wuttke, J. BornAgain: Software for Simulating and Fitting Grazing-Incidence Small-Angle Scattering. *J. Appl. Crystallogr.* **2020**, *53* (Pt 1), 262−276.

(23) Jung, F. A.; Papadakis, C. M. Strategy to Simulate and Fit 2D Grazing-Incidence Small-Angle X-Ray Scattering Patterns of Nanostructured Thin Films. *J. Appl. Crystallogr.* **2023**, *56* (Pt 5), 1330−1347.

(24) Dosch, H. Evanescent Absorption in Kinematic Surface Bragg Diffraction. *Phys. Rev. B* **1987**, *35* (5), No. 2137.

(25) Bressler, I.; Pauw, B. R.; Thünemann, A. F. McSAS: Software for the Retrieval of Model Parameter Distributions From Scattering Patterns. *J. Appl. Crystallogr.* **2015**, *48* (Pt 3), 962−969.

(26) van Herck, W.; Fisher, J.; Ganeva, M. Deep Learning for X-Ray or Neutron Scattering Under Grazing-Incidence: Extraction of Distributions. *Mater. Res. Express* **2021**, *8* (4), No. 45015.

(27) Hinderhofer, A.; Greco, A.; Starostin, V.; Munteanu, V.; Pithan, L.; Gerlach, A.; Schreiber, F. Machine Learning for Scattering Data: Strategies, Perspectives and Applications to Surface Scattering. *J. Appl. Crystallogr.* **2023**, *56* (Pt 1), 3−11.

(28) Ikemoto, H.; Yamamoto, K.; Touyama, H.; Yamashita, D.; Nakamura, M.; Okuda, H. Classification of Grazing-Incidence Small-Angle X-Ray Scattering Patterns by Convolutional Neural Network. *J. Synchrotron Radiat.* **2020**, *27* (Pt 4), 1069−1073.

(29) He, Z.; Lütgert, J.; Stevenson, M. G.; Heuser, B.; Ranjan, D.; Qu, C.; Kraus, D. Reconstruction of Nanoparticle Size Distribution in Laser-Shocked Matter From Small-Angle X-Ray Scattering via Neural Networks. *High Power Laser Sci. Eng.* **2024**, *12* (7), No. e46, DOI: 10.1017/hpl.2024.27.

(30) Simonsen, M. E.; Søgaard, E. G. Sol−Gel Reactions of Titanium Alkoxides and Water: Influence of PH and Alkoxy Group on Cluster Formation and Properties of the Resulting Products. *J. Sol−Gel Sci. Technol.* **2010**, *53* (3), 485−497.
(31) Kayser, J. J.; Arnold, P.; Steffen-Heins, A.; Schwarz, K.; Keppler, J. K. Functional Ethanol-Induced Fibrils: Influence of Solvents and Temperature on Amyloid-Like Aggregation of Beta-Lactoglobulin. *J. Food Eng.* **2020**, *270*, No. 109764.
(32) Yoshida, K.; Fukushima, Y.; Yamaguchi, T. A Study of Alcohol and Temperature Effects on Aggregation of ß-Lactoglobulin by Viscosity and Small-Angle X-Ray Scattering Measurements. *J. Mol. Liq.* **2014**, *189*, 1−8.
(33) Mousavi, S. H.-A.; Chobert, J.-M.; Bordbar, A.-K.; Haertlé, T. Ethanol Effect on the Structure of Beta-Lactoglobulin B and Its Ligand Binding. *J. Agric. Food Chem.* **2008**, *56* (18), 8680−8684.
(34) Renard, D.; Lefebvre, J.; Gobert, P.; Llamas, G.; Dufour, E. Structural Investigation of ß-Lactoglobulin Gelation in Ethanol/Water Solutions. *Int. J. Biol. Macromol.* **1999**, *26*, 35−44.
(35) Chavez, T.; Roberts, E. J.; Zwart, P. H.; Hexemer, A. A Comparison of Deep-Learning-Based Inpainting Techniques for Experimental X-Ray Scattering. *J. Appl. Crystallogr.* **2022**, *55* (Pt 5), 1277−1288.
(36) Zhou, Z.; Li, C.; Bi, X.; Zhang, C.; Huang, Y.; Zhuang, J.; Hua, W.; Dong, Z.; Zhao, L.; Zhang, Y.; Dong, Y. A Machine Learning Model for Textured X-Ray Scattering and Diffraction Image Denoising. *npj Comput. Mater.* **2023**, *9* (1), No. 58, DOI: 10.1038/s41524-023-01011-w.
(37) Roberts, E. J.; Chavez, T.; Hexemer, A.; Zwart, P. H. DLSIA: Deep Learning for Scientific Image Analysis. *J. Appl. Crystallogr.* **2024**, *57* (Pt 2), 392−402.
(38) Yin, S.; Cao, W.; Tu, S.; Liang, S.; Zou, Y.; Tian, T.; Pan, G.; Xu, Z.; Li, L.; Cheng, L.; Cheng, Y.-J.; Schwartzkopf, M.; Roth, S. V.; Zhai, L.; Müller-Buschbaum, P. Structural Evolution During Repeated Spray Deposition of $FeCl_3$-Doped Poly(Styrene)-b-Poly(4-Vinyl Pyridine) Layers. *Adv. Mater. Interfaces* **2025**, *12* (15), No. e00298, DOI: 10.1002/admi.202500298.
(39) Kaune, G.; Memesa, M.; Meier, R.; Ruderer, M. A.; Diethert, A.; Roth, S. V.; D'Acunzi, M.; Gutmann, J. S.; Müller-Buschbaum, P. Hierarchically Structured Titania Films Prepared by Polymer/Colloidal Templating. *ACS Appl. Mater. Interfaces* **2009**, *1* (12), 2862−2869.
(40) Cao, L.; Chen, D.; Li, W.; Caruso, R. A. Hierarchically Porous Titania Networks With Tunable Anatase:Rutile Ratios and Their Enhanced Photocatalytic Activities. *ACS Appl. Mater. Interfaces* **2014**, *6* (15), 13129−13137.
(41) Park, J. T.; Roh, D. K.; Patel, R.; Kim, E.; Du Ryu, Y.; Kim, J. H. Preparation of $TiO_2$ Spheres With Hierarchical Pores via Grafting Polymerization and Sol−Gel Process for Dye-Sensitized Solar Cells. *J. Mater. Chem.* **2010**, *20* (39), 8521−8530.
(42) Parkinson, D. Y.; Chavez, T.; Choudhary, M.; English, D.; Hao, G.; Hellert, T.; Leemann, S. C.; Nemsak, S.; Rotenberg, E.; Taylor, A. L.; Scholl, A.; White, A. A.; Islegen-Wojdyla, A.; Zwart, P. H.; Hexemer, A. AI@ALS Workshop Report: Machine Learning Needs at the Advanced Light Source. *Synchrotron Radiat. News* **2024**, *37* (4), 49−64.
(43) Roth, S. V.; Rothkirch, A.; Autenrieth, T.; Gehrke, R.; Wroblewski, T.; Burghammer, M. C.; Riekel, C.; Schulz, L.; Hengstler, R.; Müller-Buschbaum, P. Spatially Resolved Investigation of Solution Cast Nanoparticle Films by X-Ray Scattering and Multidimensional Data Set Classification. *Langmuir* **2010**, *26* (3), 1496−1500.
(44) Limo, M. J.; Sola-Rabada, A.; Boix, E.; Thota, V.; Westcott, Z. C.; Puddu, V.; Perry, C. C. Interactions between Metal Oxides and Biomolecules: from Fundamental Understanding to Applications. *Chem. Rev.* **2018**, *118* (22), 11118−11193.
(45) Behnajady, M. A.; Eskandarloo, H.; Modirshahla, N.; Shokri, M. Sol-Gel Low-Temperature Synthesis of Stable Anatase-Type $TiO_2$ Nanoparticles Under Different Conditions and Its Photocatalytic Activity. *Photochem. Photobiol.* **2011**, *87* (5), 1002−1008.
(46) Li, N.; Guo, R.; Oechsle, A. L.; Reus, M. A.; Liang, S.; Song, L.; Wang, K.; Yang, D.; Allegretti, F.; Kumar, A.; Nuber, M.; Berger, J.; Bernstorff, S.; Iglev, H.; Hauer, J.; Fischer, R. A.; Barth, J. V.; Müller-Buschbaum, P. Operando Study of Structure Degradation in Solid-State Dye-Sensitized Solar Cells with a $TiO_2$ Photoanode Having Ordered Mesopore Arrays. *Sol. RRL* **2022**, *6* (9), No. 2200373, DOI: 10.1002/solr.202200373.
(47) Smilgies, D.-M. Scherrer Grain-Size Analysis Adapted to Grazing-Incidence Scattering With Area Detectors. *J. Appl. Crystallogr.* **2009**, *42* (Pt 6), 1030−1034.
(48) Sydorenko, J.; Mere, A.; Krunks, M.; Krichevskaya, M.; Acik, I. O. Transparent $TiO_2$ Thin Films With High Photocatalytic Activity for Indoor Air Purification. *RSC Adv.* **2022**, *12* (55), 35531−35542.
(49) Le Bon, C.; Nicolai, T.; Durand, D. Growth and Structure of Aggregates of Heat-Denatured ß-Lactoglobulin. *Int. J. Food Sci. Technol.* **1999**, *34*, 451−465.
(50) Buffet, A.; Rothkirch, A.; Döhrmann, R.; Körstgens, V.; Abul Kashem, M. M.; Perlich, J.; Herzog, G.; Schwartzkopf, M.; Gehrke, R.; Müller-Buschbaum, P.; Roth, S. V. P03, the Microfocus and Nanofocus X-Ray Scattering (MiNaXS) Beamline of the PETRA III Storage Ring: The Microfocus Endstation. *J. Synchrotron Radiat.* **2012**, *19* (Pt 4), 647−653.
(51) Broennimann, C.; Eikenberry, E. F.; Henrich, B.; Horisberger, R.; Huelsen, G.; Pohl, E.; Schmitt, B.; Schulze-Briese, C.; Suzuki, M.; Tomizaki, T.; Toyokawa, H.; Wagner, A. The PILATUS 1M Detector. *J. Synchrotron Radiat.* **2006**, *13* (Pt 2), 120−130.
(52) Anker, A. S.; Butler, K. T.; Selvan, R.; Jensen, K. M. Ø. Machine Learning for Analysis of Experimental Scattering and Spectroscopy Data in Materials Chemistry. *Chem. Sci.* **2023**, *14* (48), 14003−14019.




https://doi.org/10.1021/acsanm.6c01622
*ACS Appl. Nano Mater.* 2026, 9, 12970−12979